Space and Planetary Resources (2025) 1:2
https://doi.org/10.1007/s44461-025-00004-5

RESEARCH

Vibration-induced size segregation of lunar regolith and simulants for in situ resource utilisation (ISRU)

J. N. Rasera[1] · L. E. Salinas-Farran[1] · S. O. Starr[1] · V. Schein[1] · B. Lomax[2] · F. McDonald[2] · J. J. Cilliers[1] · K. Hadler[1,3]

Received: 3 July 2025 / Revised: 2 September 2025 / Accepted: 30 September 2025
© The Author(s) 2025

Abstract

Effective beneficiation of lunar regolith for in situ resource utilisation (ISRU) requires size classification methods compatible with vacuum environments, where fluid-based systems are impractical. This study evaluates vibrational segregation as a dry alternative, using sealed-vial excitation under Earth gravity. We test Apollo sample 15601 alongside three lunar simulants (JSC-1, LMS-1, TUBS-M) across multiple vibrational conditions. Micro-CT imaging, Rosin–Rammler modelling, and Jensen–Shannon Divergence analysis quantify internal structure and simulant similarity. Mechanistic models of aerodynamic drag and bulk mobilisation clarify the roles of fines, cohesion, and confinement. A15601 develops a stable three-layer structure driven by fines immobilisation and coarse particle lofting. LMS-1 exhibits similar layering but weaker compaction. TUBS-M provides the closest statistical match, while JSC-1 segregates efficiently but less representatively. Particle size distribution breadth emerges as the primary driver of compaction and stratification. Though tested under terrestrial conditions, the findings offer a framework for evaluating simulants and designing passive ISRU separation systems.

Keywords ISRU · Size classification · Brazil Nut Effect (BNE) · Vibrational segregation · Micro-CT

Introduction

The regolith coating the surface of the Moon is a rich repository of potentially valuable materials, such as oxygen, metals, and water. The extraction and utilisation of these materials could serve as the foundation of a future cis-lunar economy (Kornuta et al. 2019). The process of in situ oxygen production, a key element in both rocket propellant and life support systems, has emerged as a key first target for in situ resource utilisation (ISRU) (Cilliers et al. 2023). Despite the numerous methods for oxygen extraction from lunar regolith detailed in the literature (Taylor and Carrier III 1993; Shaw et al. 2022), all demand a consistent feedstock to guarantee reliable oxygen production rates Cilliers et al. (2020). The preparation of such feedstock, referred to as beneficiation, involves processes for particle size classification and selective mineral enrichment. A review by Rasera et al. (2020) revealed that these critical-path technologies have received substantially less research attention compared to oxygen and metal production, with size classification considered infrequently.

Lunar regolith, with an average diameter (d_{50}) of 72 μm, is primarily composed of particles smaller than 1 mm, nearly a quarter of which are less than 20 μ m (Carrier III 2005; McKay et al. 1991; Rasera et al. 2020). The removal of the coarser (> 1 mm) and finer (< 90 μ m) fractions would significantly enhance the efficiency of material handling, mineral enrichment, and oxygen production processes (Cilliers et al. 2020). Besides reducing parasitic heating, blockages, and fouling, size classification can boost a reactor's efficiency and reduce its mass and power draw (Cilliers et al. 2020). Notably, it could also facilitate mineral enrichment, given the non-uniform mineralogy of regolith across different size fractions (McKay et al. 1991; Cilliers et al. 2020).

Terrestrial mining operations rely on process fluids like water or air to drive size classification operations, often using gravity-assisted methods like cyclonic separation to

✉ J. N. Rasera
j.rasera@imperial.ac.uk

[1] Department of Earth Science and Engineering, Imperial College London, London SW7 2AZ, UK

[2] European Space Research and Technology Centre (ESTEC), Keplerlaan 1, 2201 AZ Noordwijk, The Netherlands

[3] European Space Resources Innovation Centre (ESRIC), Luxembourg Institute of Science and Technology (LIST), 5, Avenue des Hauts-Fourneaux, 4362 Esch-sur-Alzette, Luxembourg

Published online: 14 October 2025

concentrate valuable minerals based on their volume, density, or mass differences relative to the fluid medium (Pukkella et al. 2023; Rasera et al. 2020). However, the lunar environment, characterised by a hard vacuum and extreme temperature variations, makes fluid-driven methods impractical. Past considerations of air cyclones and pneumatic tables for lunar size classification recognised these methods as posing “a formidable technical problem" (Williams et al. 1979).

The lunar vacuum is a complex electrostatic environment that significantly influences the dynamic behaviour of regolith (Calle 2017). This environment impacts processes such as dry sieving, where the frictional contacts experienced by particles induces triboelectric charging. While tribocharging may be used for mineral enrichment applications (e.g., Rasera et al. 2022, 2023a, 2023b; Quinn et al. 2012; Li et al. 1999; Trigwell et al. 2006, 2007, 2009, 2012; Captain et al. 2007), the resulting particle adhesion and agglomeration may impede considerably the effectiveness of sieving (Hu et al. 2021).

Vibrational segregation, also known as the ‘Brazil Nut Effect’, describes vibration-induced size segregation in granular beds. This effect, so named for the segregation of Brazil nuts to the top of a shaken mixed nut container, results in distinct layering of differently sized particles (Shinbrot 2004; Gajjar et al. 2021). Multiple mechanisms contribute to this effect, including void filling (Rosato et al. 2002; Jullien et al. 1992; Dippel and Luding 1995), convection (Duran et al. 1994; Saez et al. 2005; Huerta and Ruiz-Suárez 2004; Knight et al. 1993; Poeschel and Herrmann 1995; Shinbrot and Muzzio 1998; Möbius et al. 2001; Vanel et al. 1997), buoyancy (Sanders et al. 2004; Ciamarra et al. 2006; Huerta and Ruiz-Suárez 2004), and arching effects (Duran et al. 1994, 1993; Saez et al. 2005). Factors such as container geometry, vibration amplitude and frequency, particle size distribution, and particle surface properties influence the predominance of these mechanisms (Godoy et al. 2008). The primary mechanism is believed to be void filling, whereby smaller particles percolate into voids beneath rising larger particles, with the overburden pressure ‘locking’ the smaller particles, allowing larger ones to ascend over multiple vibration cycles (Williams 1963; Rosato et al. 1987, 2002; Chujo et al. 2017). Convection also plays a significant role in particle segregation. During vibration, frictional forces between the particles and the container walls create vertical and sideways movements within a convection cell. This movement facilitates the upward migration of larger particles (Balista et al. 2011). It has been observed that convection enables the upward migration and trapping of large particles on the bed’s surface (Duran et al. 1994; Knight et al. 1993).

Contrary to expectation, Rosato et al. (2002) found that convection could enhance particle mixing, casting doubt on its role in promoting segregation. Moreover, the authors challenged the assumption that locking of larger particles at the surface was a result of convection. Instead, they suggested that it may be induced by the void filling process. This hypothesis aligns with findings from studies on low-gravity regolith dynamics, which indicated void filling as the principal driver of segregation over convection (Maurel et al. 2016).

The broad applicability of vibrational segregation has resulted in extensive experimental and simulation studies, typically focusing on the ascension of a large ’intruder’ or the segregation of particles within monodisperse or polydisperse idealised sphere mixtures (Rosato et al. 1987; Hsiau and Yu 1997; Metzger et al. 2011; Liao 2016; Asmar et al. 2002). Few researchers have considered the application of vibrational segregation to granular systems representative of the lunar regolith. However, Kawamoto and Chin (2021) demonstrated the application of vibrational segregation to perform size segregation on 1.5 gs of lunar simulant FJS-1. They were able to segregate particles above and below 100 μm using a piezoelectrically actuated conveyor tube at different inclinations. Their findings suggest that vibrational segregation could be used effectively as a means of particle size classification on the Moon.

This study has two principal objectives: first, to evaluate the stratification and segregation behaviour of Apollo sample 15601 and three terrestrial lunar simulants (JSC-1, LMS-1, and TUBS-M) under vibrational excitation; and second, to assess which simulant most closely matches the dynamic response of the Apollo sample. Micro-CT imaging was used to resolve particle-scale changes in bed structure, while Rosin–Rammler modelling and statistical divergence methods were applied to quantify similarity. Complementary mechanistic models were introduced to interpret the roles of aerodynamic drag, cohesion, and confinement in shaping the observed behaviours. These approaches provide a novel framework for evaluating simulant geomechanical fidelity and for understanding granular material response under conditions relevant to ISRU and lunar beneficiation.

The remainder of the paper is organised as follows. Section 2 (*Sample context and significance*) motivates the choice of Apollo 15601 and the three simulants and summarises their key properties. Section 3 (*Experimental and analytical methodologies*) describes the apparatus, vibration protocols, micro-CT workflow, and the segregation and similarity metrics. Section 4 (*Results*) presents stratification patterns, axial shifts in particle size distributions, and layer-wise similarity to A15601. Section 5 (*Modelling and interpretation*) develops particle- and bulk-scale models to rationalise the observed behaviours. Section 6 (*Discussion*) considers the broader implications

for regolith mechanics and simulant use, including the effects of vibrational compaction on testing practice, and outlines limitations and future directions. Finally, Section 7 summarises the main conclusions of the study.

Sample context and significance

This study evaluates vibrational segregation behaviour in one authentic lunar regolith sample, Apollo 15 sample 15601, and three commonly used terrestrial simulants: JSC-1, LMS-1, and TUBS-M. Each material presents distinct physical and geotechnical properties (Table 1), making them suitable for comparative assessment of particle mobility, stratification, and segregation potential under Earth-based vibrational conditions.

Apollo 15 lunar soil sample 15601 is a well-characterised regolith sample collected at Station 9a, located approximately 20 m from the edge of the Hadley Rille. This site lies at the base of the Apennine Front and is geologically distinct from other sampling locations due to its proximity to both the mare and highland interfaces. The bulk sample (catalogued under 15600) had a mass of over 1.4 kg, with 15601 representing the < 1 mm sieved fraction of approximately 800 g (Morris 1983). It was retrieved using a scoop rather than a core tube or rake, and was returned in Sample Bag #7, and was stored in Apollo Lunar Sample Return Container (ALSRC) #2, which did not seal (Meyer 2011).

Sample 15601 is considered immature, with an I_s/FeO maturity index of 29 and an agglutinate content of 32% (Morris 1978). In addition to the agglutinates, the modal mineralogy is primarily composed of pyroxene (27.2%) and basaltic components (15%), with notable contributions from olivine (4.3%), plagioclase (7.5%), and minor amounts of glass (7.5%) and ilmenite (0.7%) (Basu et al. 1980). Petrographic analysis suggests that over 80% of the soil derives from olivine-normative mare basalt, consistent with its high FeO content and fine modal grain size (Meyer 2011).

Chemically, 15601 is among the most Fe-rich soils returned from the Moon, with bulk FeO values exceeding 19 wt.% (Meyer 2011). Rare earth element (REE) analyses indicate a composition dominated by mare basalt with minor KREEP (potassium, rare earth elements, and phosphorous) and green glass components. The carbon content has been reported between 72 and 95 ppm (Moore et al. 1973).

A15601's median particle size, d_{50}, is approximately 89 μ m, with a broad size distribution: $d_{10} = 8$ μ m, and $d_{90} = 1000$ μ m, based on the dataset by Graf (1993). These values reflect a heterogeneous assemblage with a significant tail of coarse fragments, likely due to micro-breccia and volcanic glass clasts embedded within the finer basaltic matrix. Given its compositional and granulometric diversity, sample 15601 is frequently employed as a reference for studies of lunar soil evolution, maturity, and mechanical behaviour.

The three simulants were selected to span a range of particle sizes, compositions, and mechanical behaviours. JSC-1 is a basaltic ash-based simulant developed at NASA Johnson Space Center to approximate the geotechnical properties of mature mare regolith, with a particular focus on cohesion, shear strength, and bulk density (McKay et al. 1994; Willman et al. 1995). While its mechanical response is broadly representative, its mineralogy and glass content diverge from actual lunar soils. LMS-1 is a mare-derived simulant

Table 1 Summary of the key physical properties of the regolith simulants and Apollo regolith sample employed in this study. The d_{10}, d_{50}, and d_{90} values represent the particle diameters at which 10%, 50%, and 90% of the cumulative mass of the sample have passed through the sieve, respectively

	Specific Gravity	Cohesion	Internal Friction	Particle Size Distribution [μ m]			References
	$[g/cm^3]$	$[kPa]$	Angle [°]	d_{10}	d_{50}	d_{90}	
A15601	3.24	1.0*	50*	8	89	1000	Carrier III et al. (1973) and Meyer (2011)
JSC-1**,***	2.91	1.0	45	22	117	450	McKay et al. (1994) and Willman et al. (1995)
TUBS-M	2.96	0.6	43.9	9	87	600	Linke et al. (2020)
LMS-1 **	2.92	0.393	34.8	7	60	170	Lab (2023), Long-Fox et al. (2023) and Long-Fox and Britt (2023)

*Values for Apollo 15 samples taken from Station 8 measurements near the landing module. In contrast, A15601 was collected at Station 9a, approximately 2 km away from Station 8 at the rim of the Hadley Rille

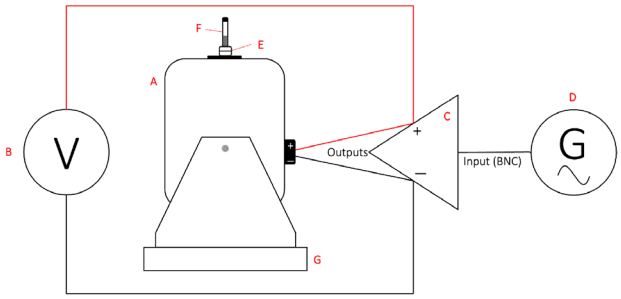
**The cohesion and friction angles evaluated by Kobaka et al. (2023) for LMS-1 and JSC-1A are different from the manufacturer-reported values: 3.2 *kPa* for LMS-1 and 5.2 *kPa* for JSC-1A; the internal friction angles were 44.2° for LMS-1 and 42.3° for JSC-1A. This is likely due to testing conditions, e.g., pre-loading, as noted by Dotson et al. (2024)

***Values for JSC-1 (used in this study) were unavailable, hence JSC-1A values are used, and are assumed to be similar to JSC-1 given their shared origin

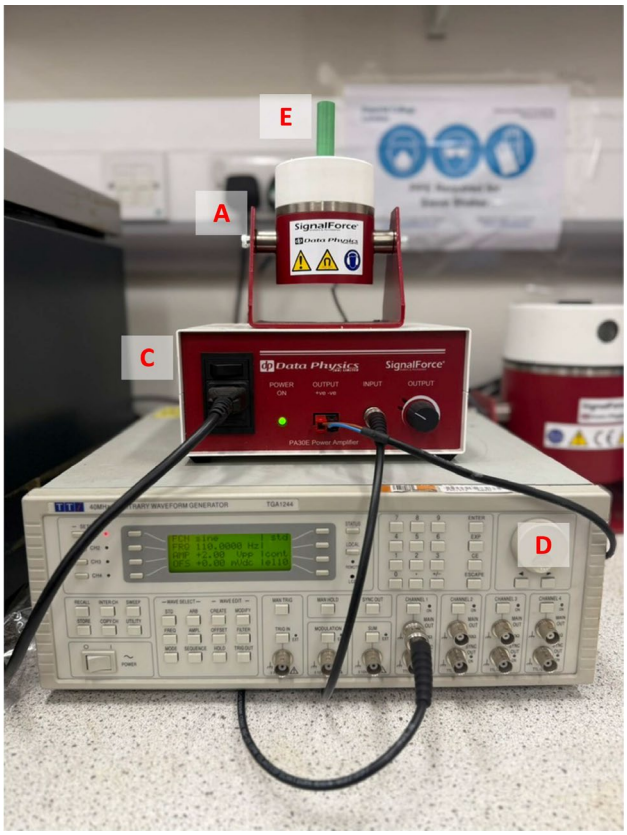
produced by the Exolith Lab,[1] formulated to match the modal mineralogy and grain size characteristics of reference mare soils (Lab 2023). It contains a significant proportion of glass-rich basalt and exhibits the finest particle size distribution of the three simulants tested, though it also has the lowest cohesion and internal friction angle. TUBS-M is a basalt-based simulant developed by TU Braunschweig with a focus on reproducing the density, flowability, and particle morphology of lunar mare regolith (Linke et al. 2020).

A recent investigation by Kobaka et al. (2023) evaluated the geotechnical performance of several lunar simulants and found LMS-1 to exhibit the closest overall similarity to averaged lunar regolith properties. JSC-1A (distinct from the JSC-1 simulant used here, but from the same source) followed closely in this comparison. While TUBS-M was not included in their study, its density and cohesion are broadly similar to those reported for Apollo 15 soils (see Table 1). Recent work by Dotson et al. (2024) has further demonstrated that both cohesion and internal friction angle vary systematically with bulk density, with cohesion increasing approximately exponentially as a function of compaction. These findings emphasise that reported values for cohesion and friction (including those listed in Table 1) are sensitive to starting density and test conditions and should therefore be considered as density-dependent rather than fixed properties.

These materials enable a systematic evaluation of vibrational segregation across different geotechnical regimes. By comparing stratification outcomes and segregation performance across samples with known differences in size, density, and cohesion, it is possible to identify which physical parameters most strongly influence mobility under vibration. The inclusion of an Apollo sample also provides a reference point against which simulant performance can be interpreted, offering insight into the limitations of terrestrial analogues and the implications for ISRU beneficiation system design.



(a) Schematic diagram showing the experimental setup. (A) Permanent magnet shaker. (B) Voltmeter. (C) Amplifier. (D) Signal generator. (E) Sample holder. (F) 2 mL glass vial containing the 1 g sample. (G) Anti-vibration mat.



(b) Photograph of the experimental setup.

Fig. 1 Experimental setup: **a** schematic diagram and **b** corresponding physical setup

Experimental and analytical methodologies

Materials

This study utilised Apollo 15 regolith sample 15601 (1.0000 g) and three widely used lunar regolith simulants: JSC-1 (1.0038 g) (McKay et al. 1994), LMS-1 (1.0015 g) (Lab 2023), and TUBS-M (1.0027 g) (Linke et al. 2020). All sample handling and preparation followed NASA-STD-1008 protocols (John and Rogers 2021). While the use of 1 g samples was necessary for consistency with the limited Apollo 15 material and to enable high-resolution CT analysis, it is important to acknowledge that such small masses may not capture the full bulk geotechnical behaviour of regolith. Bulk properties, including cohesion and frictional response, are known to vary with sample volume and packing history (Dotson et al. 2024), so the values reported here should be interpreted with this caveat in mind.

[1] Exolith Lab has since transferred its simulant production to the private start-up Space Resource Technologies; however, the sample employed in this study was procured in 2021, prior to this transition.

Experimental setup

Figure 1 illustrates the experimental apparatus used for vibrational segregation tests. Each sample was loaded into a 2-mL glass vial (50 mm in height, 9.92 mm outer diameter, 8.05 mm inner diameter) and sealed with an internal polyethylene stopper. The vials were mounted vertically in a fixed sample holder connected to a permanent magnet shaker (Data Physics GW-V20). Vertical sinusoidal excitation was driven by a signal generator (RS PRO IFG8219A 3 MHz) and amplifier (Data Physics PA30E).

Vibration amplitudes were quantified using high-speed video (Chronos 1.4, Kron Technologies) and calibrated against voltage input. Motion tracking of vial and particle trajectories was performed using the open-source software (Tracker Brown et al. 2024).

Experimental procedure

All experiments were performed at ESA ESTEC (Noordwijk, Netherlands). Sample preparation and pre-characterisation were conducted at Imperial College London.

Due to the limited availability of Apollo sample material, a single 1 g aliquot was used across all three vibration conditions. The sample was manually remixed between tests. The experimental sequence was as follows:

1. Pre-scan the mixed sample using micro-CT;
2. Mount the vial in the shaker assembly;
3. Apply the specified vibrational condition;
4. Remove and re-scan the vial using micro-CT;
5. Repeat steps 2–4 for each condition.

The vibrational conditions are summarised in Table 2. Each condition corresponds to a distinct amplitude-frequency pair. All tests were conducted for 3 min.

Micro-CT particle size analysis

X-ray micro-computed tomography (micro-CT) was used to characterise internal structure and particle size distributions. Scans were conducted using a Phoenix V|tome|x system at 100 kV and 110 μA, with an exposure of 1000 ms per frame and 500 projections over a full 360° rotation. The resulting volumetric reconstructions achieved a linear resolution of 3.7 µ m. Approximately, 20% of the total particles fell below the detection threshold.

Segmentation was performed using the Otsu algorithm to distinguish the particles from the glass container (Otsu 1979), followed by the maximum entropy method to extract particles from the background (Skilling and Bryan 1984). To minimise wall effects, a cylindrical core of 1.85 mm diameter (approximately 23% of the total vial cross-section) was selected from the centre of the column (Fig. 2). This subset was used for the subsequent computational analysis.

Each extracted core was divided into five contiguous axial layers. Individual particles were labelled using a three-dimensional 18-neighbour connectivity algorithm. Particle diameter was estimated from the volume of each labelled object, allowing a particle size distribution (PSD) to be calculated for each layer. Only particles larger than 20 µ m were included in the PSD analysis. Measured d_{50} values were compared to published data for each material to assess fidelity.

Segregation and similarity metrics

To capture both parametric characterisation of particle size distributions and non-parametric assessment of their divergence, two complementary approaches were employed: (i) Rosin–Rammler distribution fitting, and (ii) Jensen–Shannon divergence (JSD) analysis. JSD was chosen in preference to alternatives such as the Kolmogorov–Smirnov statistic because it provides a symmetric, bounded, and scale-invariant measure of distributional difference, which is well suited for comparing stratified sub-volumes on a common basis.

Table 2 Peak accelerations computed from sinusoidal vibration with displacement amplitude A and frequency f

Frequency (Hz)	Amplitude (mm)	Peak acceleration (m s^{-2})	Peak acceleration (g)
15	11.90	105.7	10.8
30	6.40	227.4	23.2
70	0.82	158.6	16.2

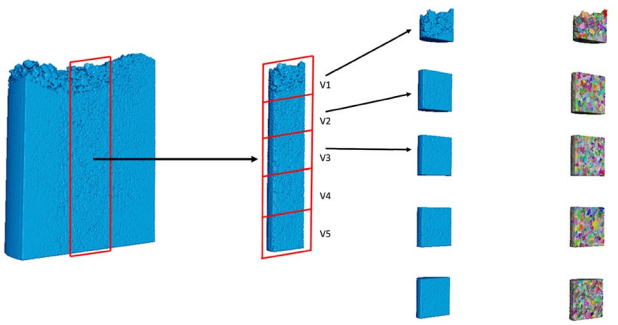


Fig. 2 Procedure for extracting and subdividing the cylindrical core into five axial layers; the PSD for each sub-volume was determined to evaluate the segregation behaviour of the sample (see Figs. 5 and 6). Each particle was labelled using 18-neighbour connectivity for particle-wise PSD estimation

The cumulative particle size distribution in each sub-volume was fitted using the Rosin–Rammler function (Plitt and Kawatra 1979):

$$F(d) = 1 - \exp\left(-0.693\left(\frac{d}{d_0}\right)^n\right), \quad (1)$$

where $F(d)$ is the mass fraction of particles with diameter $\leq d$, d_0 is the characteristic size, and n describes the spread of the distribution.

Fitting was performed using a non-linear least squares algorithm (`scipy.optimize.curve_fit`), with root-mean-square error (RMSE) and R^2 used to evaluate goodness-of-fit. The Rosin–Rammler distribution was selected because its two-parameter form provides a compact but widely validated description of comminuted granular systems and is frequently employed in mineral processing and size distribution studies.

To compare PSDs across samples and conditions, the JSD was calculated between the layer-wise distributions. The JSD is a symmetric and bounded measure (0 for identical, 1 for completely dissimilar) derived from the Kullback–Leibler divergence (Cover 1999; Nielsen 2020). For two discrete, normalised probability distributions P and Q, the JSD is

$$\mathrm{JSD}(P \parallel Q) = \frac{1}{2}D_{\mathrm{KL}}(P \parallel M) + \frac{1}{2}D_{\mathrm{KL}}(Q \parallel M), \quad (2)$$

where $M = \frac{1}{2}(P + Q)$ and

$$D_{\mathrm{KL}}(P \parallel M) = \sum_i P(i) \log \frac{P(i)}{M(i)}. \quad (3)$$

All distributions were normalised prior to divergence calculation. JSD was chosen over alternatives such as the Kolmogorov–Smirnov statistic because it yields a symmetric, scale-invariant similarity metric that is less sensitive to localised bin fluctuations, enabling robust comparison of stratified sub-volumes on a common [0,1] scale.

Permutation testing (1000 iterations) was used to assess the statistical significance of each JSD result, allowing hypothesis testing against the null model of random distribution similarity (Good 2013). The test was implemented by pooling the two particle size distributions under comparison, randomly shuffling their labels, and partitioning them into two pseudo-samples. For each iteration, kernel density estimates were constructed for the permuted samples and a new JSD value was calculated. Repeating this procedure 1000 times generated a null distribution of JSD values. The observed JSD was used as the test statistic, and the empirical p value was defined as the fraction of permuted JSDs greater than or equal to the observed JSD. A significance threshold of $\alpha = 0.05$ was applied when interpreting results.

The methodologies described above provide a high-resolution view of particle-scale segregation and bulk stratification under vibrational excitation. By combining micro-CT particle labelling with Rosin–Rammler modelling and JSD-based statistical comparison, it is possible to quantitatively assess the separation performance of each sample. These metrics serve as the basis for the analysis presented in the following section, where both qualitative and quantitative evidence of segregation behaviour are evaluated and compared across all materials and vibration conditions.

Results

This section presents the experimental outcomes of vibrational segregation tests across the Apollo 15 regolith sample and three terrestrial simulants. The analysis is structured to (i) evaluate the extent and character of stratification observed in each material, (ii) assess changes in particle size distributions following vibration, and (iii) compare simulant responses to A15601 using statistical similarity metrics. These results provide a basis for interpreting material-specific behaviours under sealed, Earth-gravity conditions.

Stratification patterns and bed compaction

Figure 3 presents XZ cross-sections from micro-CT scans for each material before vibration and after exposure to the three vibrational conditions (15, 30, and 70 Hz). Each sample exhibits some degree of vertical particle redistribution, with stratification becoming more pronounced at higher frequencies.

The Apollo 15 sample, A15601, developed a reproducible three-layer structure. Coarse particles accumulated at the top, a compacted intermediate layer formed beneath, and finer particles settled at the base. This layered architecture became more distinct as frequency increased, with the coarse layer reaching a maximum thickness of 1.13 mm after shaking at 70 Hz.

TUBS-M exhibited limited segregation. At 15 and 30 Hz, no clear separation of particle sizes was observed, and only mild upward migration of coarser particles occurred at 70 Hz. Over 90% of the sample remained static throughout the test sequence, suggesting strong internal resistance to motion.

JSC-1 displayed classical two-layer segregation behaviour. A clear upper layer of coarse particles developed, particularly at 70 Hz, where particles larger than 1.8 mm were observed at the surface.

LMS-1 responded similarly to A15601, producing three visible layers at each frequency. The internal stratigraphy of LMS-1 was also consistent across runs, indicating stable separation dynamics.

All samples exhibited compaction relative to their initial bed height (Fig. 4). Materials with broad particle size

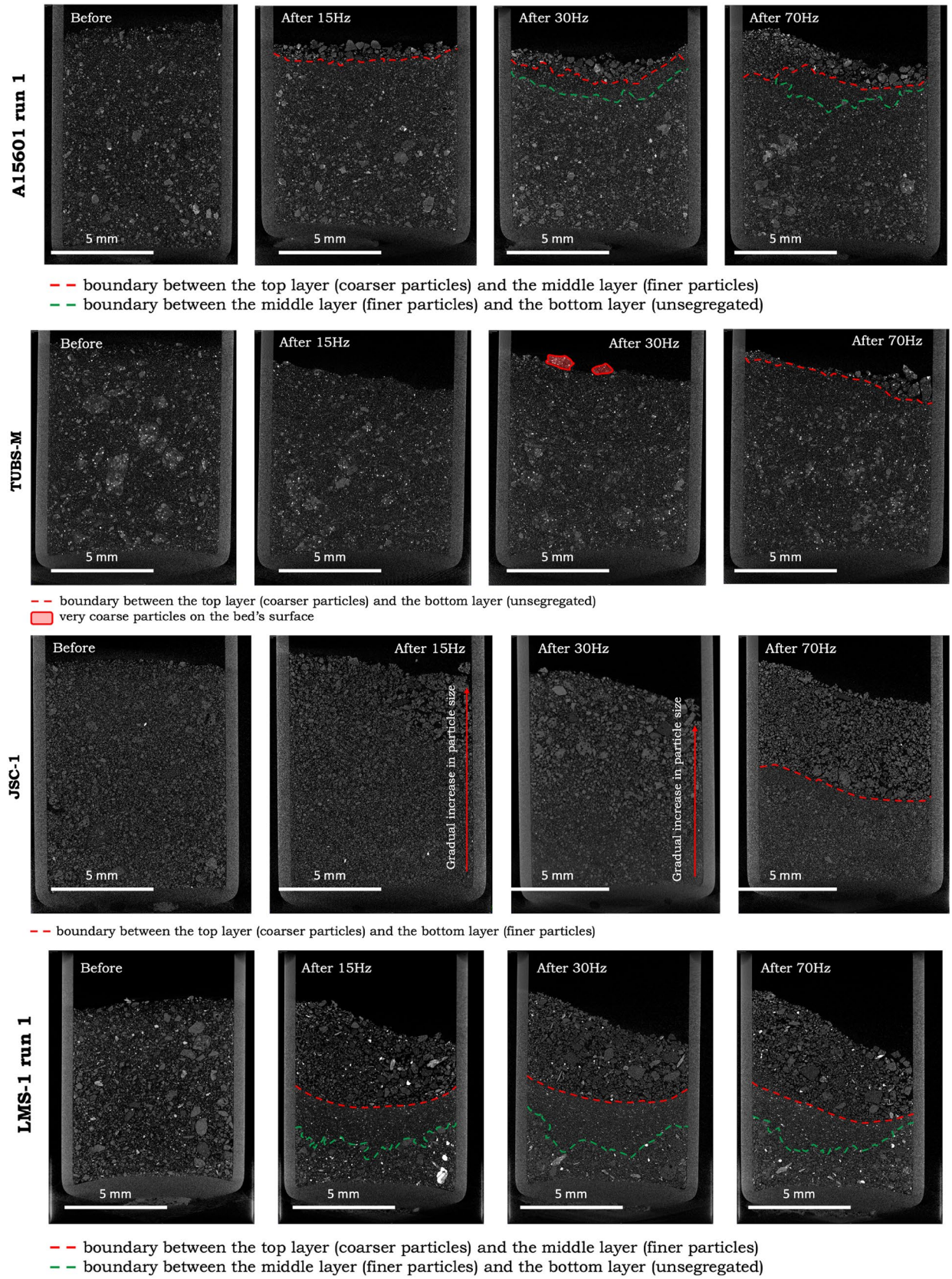


Fig. 3 Micro-CT scans of each sample before shaking, and after shaking at 15, 30, and 70 Hz. Boundaries were determined manually from the micro-CT images

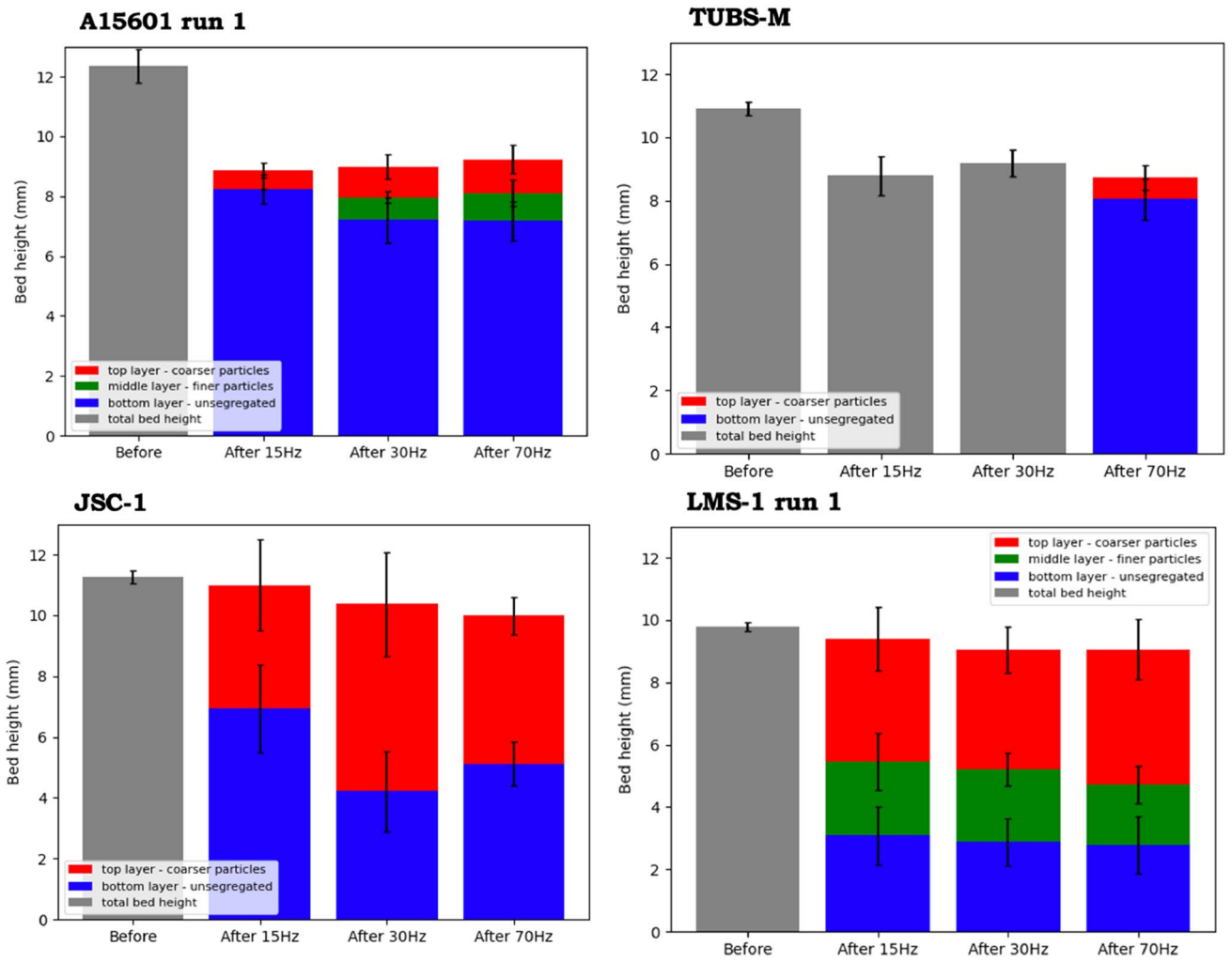


Fig. 4 Comparison of bed heights and layer thicknesses after each vibrational condition. Layer thicknesses were determined by averaging six measurements on two cross-sections extracted from the micro-CT scans

distributions, such as A15601 and TUBS-M, exhibited the greatest compaction, likely due to finer particles settling into voids between coarser grains. In materials with finer, narrower distributions, like LMS-1, lower voidage and internal cohesion appear to resist densification. At higher frequencies, convective motion of coarse particles was observed visually during operation, contributing further to compaction in the lower layers.

Axial shifts in particle size distributions

To assess segregation at higher resolution, each vial was subdivided into five axial layers, and the Rosin–Rammler parameters d_0 (mean diameter) and n (spread) were calculated for each sub-volume. Results are shown in Fig. 5, with marker colours indicating n.

Prior to shaking, all materials showed near-uniform d_0 values across layers, indicating consistent mixing. After vibration at 15 Hz, A15601 and JSC-1 began to show slight gradients in d_0, with lower layers exhibiting smaller mean particle diameter. At 30 Hz, segregation intensified, particularly in TUBS-M, which showed a sharp decrease in d_0 between adjacent layers, suggesting strong vertical sorting.

At 70 Hz, the d_0 values for TUBS-M largely returned to pre-shake levels, though with narrower PSDs, indicating densification without continued separation. In contrast, JSC-1 and LMS-1 showed levelling in d_0 across middle and upper sub-volumes, consistent with surface accumulation of coarse particles. A15601 remained comparatively unchanged from 30 Hz to 70 Hz, with only minor refinement in PSD shape.

These results confirm that vibrational frequency influences both the magnitude and pattern of segregation. This suggests that materials with broad PSDs or greater fines content (A15601, LMS-1) exhibit stratification

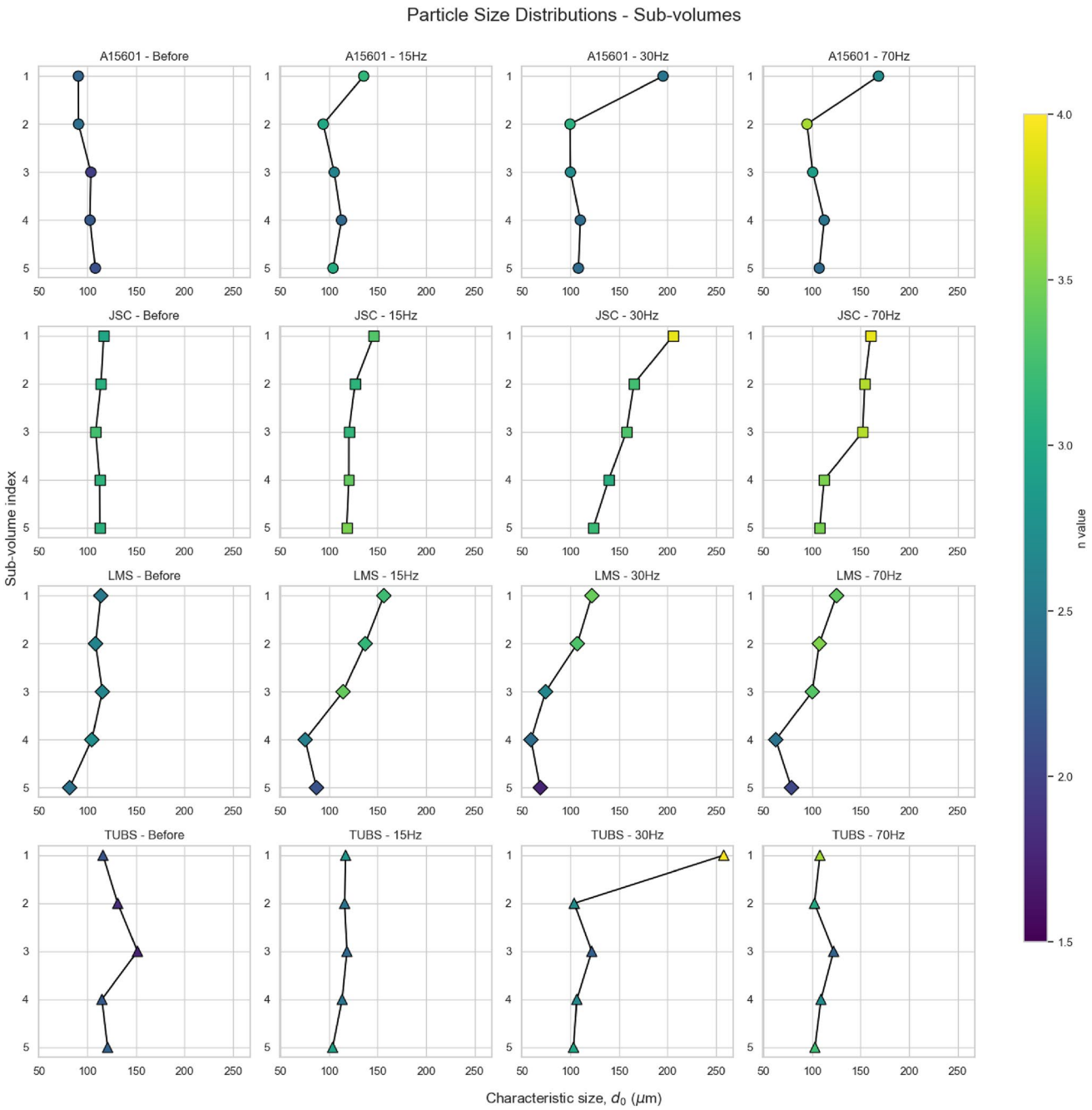


Fig. 5 Summary of the d_0 values for each material within each axial slice (see Fig. 2). The marker colour is related to the Rosin–Rammler spread parameter, n

stabilised by cohesive or jammed intermediate layers, and those with larger grain sizes and fewer fines (e.g., JSC-1) tend toward more efficient segregation. Furthermore, the d_0 values extracted from the micro-CT analysis align reasonably well with the values reported in Table 1, despite the resolution limitations.

Simulant similarity to A15601

Figure 6 shows heatmaps of Jensen–Shannon divergence (JSD) values and associated p values for each simulant compared with A15601, computed layer-by-layer across all vibration conditions. Lower JSD values reflect greater similarity in the PSD. JSD values below 0.1 with $p > 0.05$

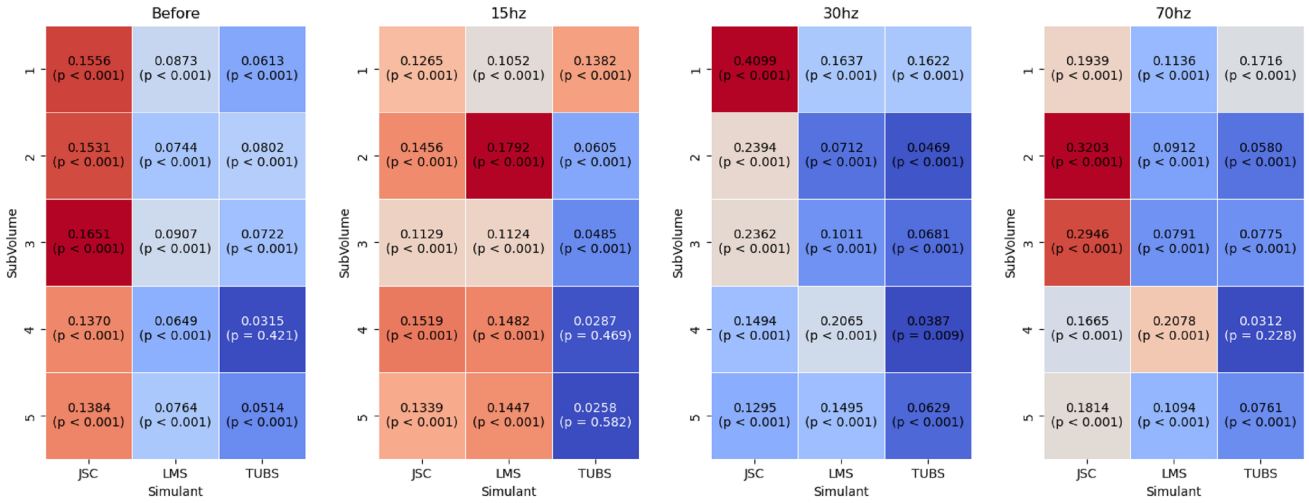


Fig. 6 Heatmap representations of the JSD values (top number) and p values (bottom number) for each sub-volume (see Fig. 2) and frequency condition. JSD values below 0.1 (blue) indicate greater similarity to A15601; value above 0.1 (red) indicate dissimilarity. Cases with $p > 0.05$ indicate statistically insignificant differences between simulant and A15601

are considered statistically indistinguishable from the Apollo sample.

TUBS-M consistently yielded the closest match to A15601, particularly in the middle and lower sub-volumes. LMS-1 followed closely, with moderate divergence in the lower layers. JSC-1 produced higher JSD values in nearly all cases, with all differences being statistically significant.

These results highlight TUBS-M as the most dynamically representative of A15601 in sealed, vibrated environments, despite its omission in recent geotechnical benchmarking studies. LMS-1 provides the closest match in terms of stratification behaviour, but its lower friction angle and cohesion may limit its fidelity under certain flow or compaction regimes.

Modelling and interpretation

To interpret the experimentally observed segregation behaviours, this section develops a mechanistic framework describing particle- and column-scale responses to sinusoidal vibration in a sealed system. These models are not intended to replicate experimental outcomes directly, but rather to clarify the physical interactions, particularly those involving air drag and confining geometry, that govern the onset and extent of particle motion. Two complementary approaches are used: a particle-scale drag model to explore lift-off thresholds for fine grains; and, a bulk force balance model to examine the onset of column mobility.

Particle-scale drag and lift-off thresholds

Under vibrational excitation in sealed containers, particles were subjected both to inertial forces from the vessel motion and to drag induced by pressure-driven air flow. This effect was most pronounced for fine particles, which experience disproportionately high aerodynamic resistance. To examine this behaviour, we developed a particle-scale model describing the balance between inertial launch and drag damping.

The displacement, velocity, and acceleration of the vial were defined as sinusoidal functions of amplitude α and angular frequency ω, with lift-off assumed to occur during downward deceleration. The initial particle velocity was approximated as $v_i \approx \alpha\omega/2\pi$. Air flow generated by the oscillating vial was represented using an axisymmetric approximation with a Bessel-derived scaling term Γ (see Appendix A). The resulting particle equation of motion incorporated Stokes drag, with closed-form solutions obtained via Laplace transforms (coefficients given in Appendix A).

Model outputs indicated that fines ($\lesssim 20\ \mu$m) rapidly lost momentum due to drag coupling with the surrounding air and therefore failed to reach ballistic motion, even when inertial thresholds were exceeded. By contrast, coarser particles experienced minimal damping and were consistently lofted, reproducing the observed upward migration of large grains in A15601 and LMS-1. Figure 7 compares predicted trajectories in air and vacuum, while Fig. 8 illustrates agreement between model predictions and experimental videography at 15 Hz. These results highlight that fines immobilisation is an intrinsic outcome of sealed, air-filled conditions

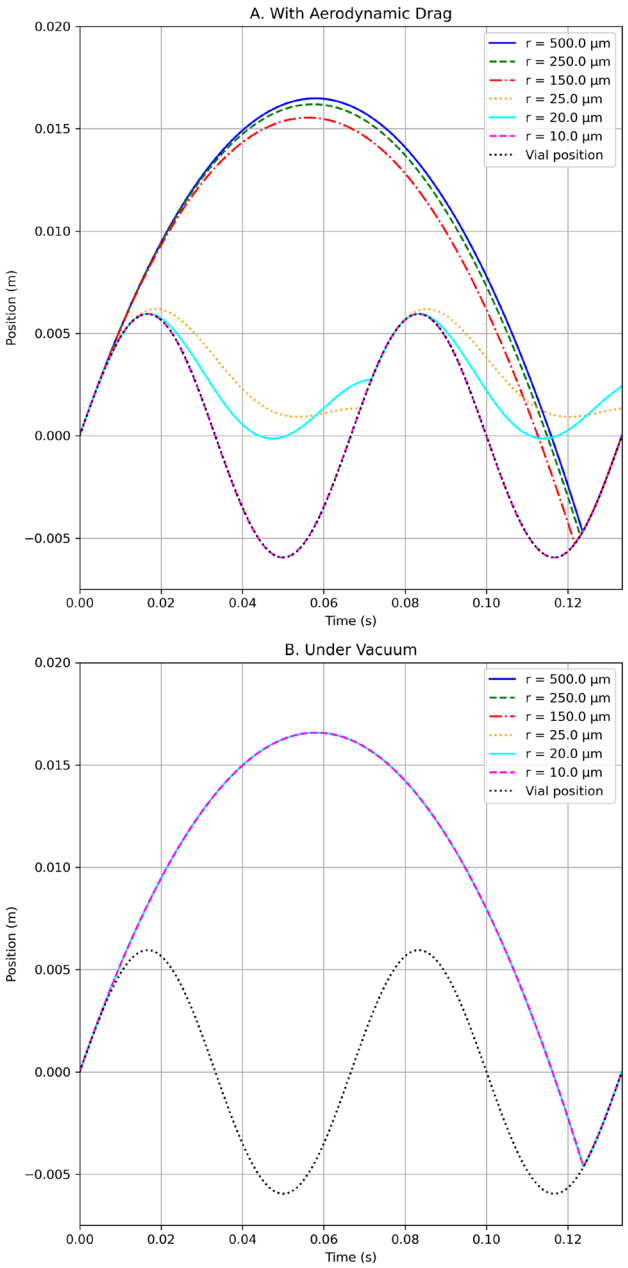


Fig. 7 **A** Calculated vertical displacement versus time for A15601 particles under atmospheric conditions. **B** The same particles and vibrational characteristics, but under vacuum conditions

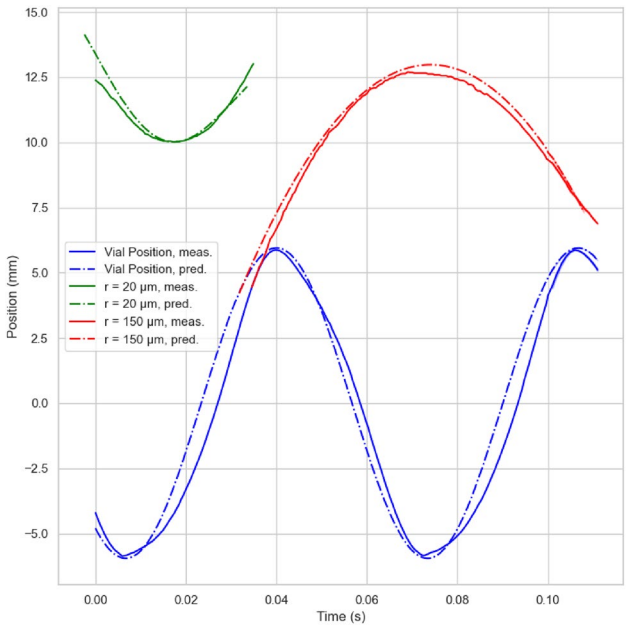


Fig. 8 The measured and predicted vertical (y) position of two A15601 particles and the vial as function of time. The measured trajectories were plotted using slow-motion videos and Tracker (Brown et al. 2024). These data were taken from a 15 Hz experiment. The relatively high position of the $r = 20\mu m$ particle was likely due to entrainment with larger particles as they were lofted. Since the model does not account for multiple particles, the position of predicted curve was shifted to more easily compare the shape of the trajectory

and provides a mechanistic basis for the layered stratigraphy observed in CT analyses.

Bulk motion thresholds and confinement effects

To complement the particle-scale analysis, a bulk force balance model was applied to evaluate the threshold for column-scale motion in confined geometries. Following the Janssen effect (Nielsen 1998), vertical loads in granular beds are partially transferred to container walls, reducing basal stress and impeding downward flow.

For a horizontal slice of thickness dz, equilibrium yields

$$R(\sigma_{zz}(z+dz) - \sigma_{zz}(z)) = \rho g R dz - 2dz\gamma\sigma_{rr}, \tag{4}$$

where R is the column radius, σ_{zz} is the vertical stress, σ_{rr} is the radial stress, and γ is the wall friction coefficient. Assuming $\sigma_{rr} = K\sigma_{zz}$, this expression reduces to

$$\frac{d\sigma_{zz}}{dz} = \rho g - \frac{2K\gamma}{R}\sigma_{zz}, \tag{5}$$

with solution:

$$\sigma_{zz}(z) = \frac{\rho g R}{2K\gamma}\left(1 - e^{-\frac{2K\gamma}{R}z}\right). \tag{6}$$

Using a Janssen coefficient $K\gamma = 0.16$ (Arens and Starr 2012), the characteristic length scale for stress saturation was estimated at 13 cm, confirming the validity of a hydrostatic approximation for the present sample heights. The onset of bulk motion is controlled by the ratio of vibrational to gravitational acceleration,

$$\Lambda = \frac{A\omega^2}{g}, \tag{7}$$

with mobilisation expected when $\Lambda \geq 1$ (Duran 2012). Extending the force balance to include wall friction and Mohr–Coulomb cohesion gives the critical threshold:

$$\Lambda_{crit} = 1 + \frac{h_{total}}{R} K\gamma + \frac{c}{\rho g h_{total}}, \tag{8}$$

where h_{total} is the bed height, ρ the bulk density, and c the cohesion. Parameter values from Table 1 yield predicted thresholds of 3.34 (A15601), 3.58 (JSC-1), 2.62 (TUBS-M), and 2.16 (LMS-1).

This framework clarifies how confinement, cohesion, and wall friction influence mobilisation, but it neglects particle–particle interactions. Real regolith grains are angular, polydisperse, and electrostatically active. These properties increase resistance to motion relative to the simplified model: electrostatic adhesion can cluster fines and suppress ballistic ejection even when $\Lambda \geq 1$, while interlocking creates stress transmission pathways not captured by the Janssen approximation. At the same time, local rearrangements or arch collapse may generate intermittent flow below threshold accelerations. More realistic treatments incorporating density-dependent shear strength (Dotson et al. 2024), as well as discrete element or coupled electro-mechanical simulations, would provide a fuller account of regolith dynamics.

Comparison with experiments highlights these limitations. TUBS-M, despite its low cohesion and narrow PSD, exhibited pronounced stratification at 30 Hz that dissipated at higher frequencies. LMS-1, predicted to mobilise most readily due to its low Λ_{crit}, showed only weak segregation with limited divergence in d_0 across sub-volumes. These discrepancies emphasise that fines content, PSD breadth, and drag effects contribute strongly to dynamic responses and cannot be explained by bulk force balance alone.

Linking model insights to material behaviour

The two models clarify the dual roles of aerodynamic drag and interparticle forces in governing segregation behaviour under sealed, vibrational conditions. Fine particles are immobilised by both low inertia and their strong coupling to the surrounding air. This drag-mediated effect is absent in vacuum but highly relevant in terrestrial analogue testing. Aerodynamic suppression helps explain the persistent fines-rich lower layers observed in A15601 and LMS-1, both of which contain substantial sub-20 µm fractions.

At the bulk scale, wall friction and cohesion define a theoretical threshold for column mobilisation. However, the experimental results suggest that crossing this threshold does not guarantee mobilisation. TUBS-M, despite exhibiting a broad PSD and relatively low cohesion, displayed transient axial separation at 30 Hz that largely dissipated by 70 Hz. Conversely, LMS-1, which has the narrowest PSD and lowest friction angle, maintained relatively uniform profiles across frequencies, with minimal further stratification at high excitation.

These behaviours underscore that vibrational segregation in confined, sealed systems is governed not solely by granulometry or bulk strength, but by dynamic feedbacks between particle-fluid coupling, drag damping, and fines-induced jamming. The dual modelling approach presented here provides a framework for interpreting these effects, highlighting the need to consider both material-specific drag susceptibility and the evolving internal structure of the granular bed.

Discussion

The results presented here confirm that vibrational segregation behaviour is highly material-dependent, shaped by a combination of particle-scale dynamics, bulk mechanical properties, and aerodynamic forces within sealed systems. While all four samples exhibited some degree of stratification under harmonic excitation, the nature and extent of this segregation varied substantially. These differences can now be contextualised using the mechanistic models described in Sect. 5.

Fine particle immobilisation and drag suppression

The experimental data show that A15601 and LMS-1 both develop a three-layer structure with fines concentrated at the base. The particle-scale model reveals that aerodynamic drag acts as a critical inhibitory mechanism for small particles in sealed containers. Particles below ~20 µ m, which constitute a substantial portion of both A15601 and LMS-1, are predicted to be strongly coupled to the downward-moving air column during vessel lift. As a result, they lose momentum rapidly and fail to achieve lift-off.

This aerodynamic trapping is absent in vacuum, as shown in the comparative trajectories of Fig. 7, and would therefore not be relevant in lunar environments. However, under Earth-based experimental conditions, this effect contributes meaningfully to the development of a stratified architecture, particularly in materials with broad particle size distributions and high fines content.

Bulk mobility, confinement, and cohesion effects

The bulk force balance model provides a first-order estimate of the excitation required to initiate column lift, based on cohesion, geometry, and wall friction. However, the transition from bulk motion to meaningful segregation is shaped

by additional factors, including particle shape, fines content, and PSD breadth. All four materials experienced some degree of compaction under vibration, but the relationship between mobilisation and stratification varied substantially.

A15601, with high density and moderate cohesion, exhibited the strongest compaction and clearest three-layer structure. Its broad PSD and high fines content facilitated void filling and aerodynamic damping, contributing to the development of a stable, jammed intermediate zone beneath a coarse surface layer.

LMS-1, while predicted to be the easiest to mobilise based on its low Λ_{crit}, cohesion, and internal friction, showed comparatively weak segregation. Although stratification patterns were visible in CT slices, the d_0 gradients were modest, and PSD convergence across sub-volumes indicated limited differential motion. This may reflect an insufficient force imbalance across its narrower PSD, or a tendency toward rapid remixing due to low internal friction.

TUBS-M, which shares a similarly broad PSD with A15601 but has higher internal friction, displayed sharp axial separation at 30 Hz, but this stratification dissipated at 70 Hz. Its relatively low cohesion and moderate Λ_{crit} suggest the column was easily mobilised, but the lack of sustained separation implies that remixing dominated over stable layer formation at high frequencies.

In contrast, JSC-1, despite its higher cohesion and moderate Λ_{crit}, segregated consistently across all frequencies. Its PSD with low fines content likely enabled efficient void filling and ballistic motion, with fewer drag-related constraints acting on fine particles.

These results reinforce that bulk mobilisation is a necessary but not sufficient condition for vibrational segregation. The formation and persistence of stratified layers depend on how internal gradients, mediated by PSD shape, fines fraction, and drag sensitivity, interact with the imposed excitation.

Segregation trends and simulant comparisons

While all three simulants differ in composition from A15601, their stratification responses offer useful comparative insights. LMS-1 showed the greatest visual and structural similarity to A15601, including the emergence of a jammed intermediate layer. TUBS-M, meanwhile, displayed the closest statistical match in Jensen–Shannon divergence metrics, particularly in the upper and middle sub-volumes. This suggests that dynamic similarity may not always correspond with visual or stratigraphic similarity and underscores the need for multi-faceted assessment frameworks.

JSC-1 diverged most strongly from A15601 across all metrics. Its segregation behaviour more closely resembled that of a synthetic bimodal system, with a sharp interface between coarse and fine fractions and little indication of intermediate stratification. This difference is likely attributable to its lower fines content and narrower PSD tail, which reduce drag effects and promote clean separation.

Interpreting bed height and compaction patterns

The compaction behaviour observed in Fig. 4 closely mirrors the breadth of each sample's particle size distribution. A15601, with the widest range of particle sizes ($d_{90}/d_{10} = 125$), exhibited the most pronounced compaction, with the bed height decreasing by more than 3 mm across all vibrational conditions. TUBS-M, with a similarly broad PSD ($d_{90}/d_{10} = 67$), also compacted substantially, though to a lesser extent.

In contrast, JSC-1 and LMS-1, both with narrower PSDs ($d_{90}/d_{10} = 20.5$ and 24.3, respectively), showed only modest compaction. LMS-1 in particular exhibited minimal bed height reduction, remaining largely unchanged even at higher excitation frequencies.

These trends indicate that the availability of finer particles to fill interstitial voids beneath larger grains is the dominant factor driving compaction in sealed, vibrated beds. Broader PSDs facilitate more efficient packing as vibration encourages fines to migrate downward into pore spaces. Materials with narrower PSDs lack this void filling capacity and thus exhibit limited dynamic reorganisation once initially settled.

Other geotechnical properties, such as cohesion, internal friction, and bulk density, show no consistent correlation with the degree of compaction observed. This suggests that, under the sealed and vertically vibrated conditions employed here, particle size distribution breadth is the primary control on bed densification.

These observations have direct implications for laboratory practices where vibration is deliberately used to compact simulant beds prior to testing. While such preparation is often intended to create a homogeneous target density, the results here show that vibration can simultaneously drive size-dependent segregation and depth-dependent density variation. As a result, beds produced by vibrational compaction may not be uniform, but instead exhibit gradients in shear strength and bearing capacity with depth. This could influence outcomes in cone penetration, shear box, wheel mobility, or excavation tests, where assumptions of homogeneity underpin data interpretation. Recognising and accounting for this potential stratification is therefore important both in designing laboratory tests and in extrapolating their results to operational conditions.

Implications for ISRU and simulant use

The vibrational method described here offers a new means of assessing material behaviour relevant to ISRU beneficiation processes, particularly in feedstock preparation

and dry separation systems. By combining high-resolution micro-CT with statistically rigorous comparison metrics, this approach captures both local and global segregation dynamics in a format relevant to engineering design.

The results suggest that simulant selection should not be based solely on averaged geotechnical properties. LMS-1, for example, performed well in terms of stratification structure, but based on the JSD analysis, TUBS-M offered a better match in statistical similarity to the behaviour of A15601. JSC-1, while widely used, may be less appropriate for applications where fines-rich, stratified behaviour is expected. These findings support the need for multi-dimensional simulant characterisation and selection criteria tailored to specific operational requirements.

Limitations and future directions

The current experimental configuration (sealed vials under Earth gravity) necessarily introduces constraints that limit extrapolation to lunar or Martian environments. Air drag, which plays a central role in fine particle behaviour here, would be absent or reduced in vacuum or low-pressure conditions. Similarly, the confining geometry of the vial introduces boundary effects not present in large-scale systems.

Nonetheless, the mechanistic models presented in Sect. 5 provide a pathway to reinterpret these results under altered environmental conditions. With suitable modification, the approach could be extended to reduced-gravity testing or applied in scaled analogue rigs. Further work could also explore how cohesion and electrostatic effects evolve under different atmospheric conditions, as these may dominate segregation thresholds in lunar applications.

An additional limitation arises from the use of 1 g samples. While this choice was dictated by the available Apollo material and by the need for direct comparability between regolith and simulant datasets, small-sample masses may not fully reproduce bulk mechanical behaviour. As recent work has shown, geotechnical parameters such as cohesion and shear strength exhibit dependence on both density and sample volume (Dotson et al. 2024). Larger returned regolith allocations will ultimately be required to validate small-sample observations and to reduce uncertainty in extrapolating laboratory-scale results to operational contexts in lunar exploration and ISRU.

Finally, while the Rosin–Rammler and JSD approaches provide strong quantitative tools, further development of three-dimensional metrics, for example, based on local particle packing or contact networks, could enhance future comparison studies and refine simulant selection frameworks.

Conclusion

This study presented the first direct comparison of vibrational segregation behaviour in Apollo regolith and widely used lunar simulants, using sealed-vial excitation under Earth gravity. Through a combination of micro-CT imaging, Rosin–Rammler modelling, and statistical similarity analysis, we quantified the extent and nature of segregation across a range of excitation conditions.

While all samples exhibited measurable changes in bed height and internal layering, the response varied markedly between materials. A15601 developed a reproducible three-layer structure with pronounced fines immobilisation and a coarse surface cap. LMS-1 exhibited similar stratification, albeit with lower overall cohesion. JSC-1 showed classical two-layer segregation with sharp particle size transitions, and TUBS-M largely resisted separation under all conditions. These behaviours are attributable to differences in particle size distribution, fines content, and internal friction, rather than any single parameter alone.

The particle- and bulk-scale models introduced here provide explanatory context for these behaviours. Aerodynamic drag within the sealed vial was found to suppress the mobility of fine particles, particularly in samples with high fines content and broad PSDs. Bulk mobility thresholds, by contrast, were governed by a combination of cohesion, column geometry, and wall friction. These mechanisms together account for the emergence of jammed intermediate layers in A15601 and LMS-1, and the limited response of TUBS-M to vibrational excitation.

TUBS-M was found to be the most statistically similar to A15601 in terms of particle size distribution within subvolumes, although LMS-1 more closely matched its layered structure. JSC-1 diverged significantly from A15601 across all metrics. These results suggest that simulant selection for ISRU process development should consider dynamic stratification behaviour alongside static geotechnical benchmarks.

Despite the sealed, Earth-gravity constraints of this study, the experimental approach offers a novel and practical framework for evaluating segregation potential in granular materials. Future work could extend this method to reduced-pressure and reduced-gravity environments, or integrate it with complementary flow and cohesion tests to support simulant validation. The data presented here provide a reference point for such efforts and offer new insights into the mechanisms governing particle motion in lunar soil analogues.

Appendices

Derivation of fluid velocity

We assume that the air in the vial is viscous and incompressible, and that the air flow is fully developed, axisymmetric, and driven by an oscillatory pressure gradient. Given these assumptions, the Navier–Stokes equation can be written as

$$\rho_f \frac{\partial v_y(r,t)}{\partial t} = -\frac{\partial P(y,t)}{\partial y} + \mu\left(\frac{1}{r}\frac{\partial}{\partial r}\left(r\frac{\partial v_y(r,t)}{\partial r}\right)\right) \tag{9}$$

The pressure gradient can be expressed in complex form as

$$\frac{\partial P(y,t)}{\partial y} = \partial P_0 e^{i\omega t}, \tag{10}$$

where P_0 is the maximum amplitude of the oscillating pressure gradient.

The velocity can be decomposed by separation of variables into radial and time-dependent parts by

$$v_y(r,t) = V(r)e^{i\omega t} \tag{11}$$

By substitution of 10 and 11 into 9, we find

$$\rho_f i\omega V(r) = -\Delta P_0 + \mu\left(\frac{1}{r}\frac{\partial}{\partial r}\left(r\frac{\partial V(r)}{\partial r}\right)\right) \tag{12}$$

The Womersley number, $\Omega = r_{vial}\sqrt{\frac{\rho_f \omega}{\mu}}$, is a non-dimensional measure of the unsteadiness of the flow. Flows where $\Omega < 1$ tend to be dominated by viscous forces, whereas those where $\Omega > 1$ are dominated by inertial forces. We then define a coefficient of convenience, $\beta = \frac{\Omega}{r_{vial}}\sqrt{i}$. By re-arranging the governing Eq. 12 for $V(r)$, and substituting in β, we find

$$\frac{1}{r}\frac{\partial}{\partial r}\left(r\frac{\partial V(r)}{\partial r}\right) - \beta^2 V(r) = \frac{\Delta P_0}{\mu} \tag{13}$$

The homogeneous form of Eq. 13 is a Bessel differential equation with the solution:

$$V_{homogeneous}(r) = C_1 J_0(\beta r) \tag{14}$$

Because the right-hand side of Eq. 13 is independent of r, we assume the particular solution of the equation is

$$V_{particular}(r) = \frac{\Delta P_0}{\mu\beta^2} \tag{15}$$

As we have assumed no-slip conditions at the boundaries, $V(r_{vial}) = 0$. Thus, the general solution is given by

$$V(r) = \frac{\Delta P_0}{\mu\beta^2}\left(1 - \frac{J_0(\beta r)}{J_0(\beta r_{vial})}\right) \tag{16}$$

Re-introducing the time-dependence results in the Womersley flow solution:

$$v(r,t) = \frac{\Delta P_0}{\mu\beta^2}\left(1 - \frac{J_0(\beta r)}{J_0(\beta r_{vial})}\right)e^{i\omega t} \tag{17}$$

Because the fluid velocity is real and oscillatory, we are interested in the real components of the solution only. The maximum fluid velocity, v_{max}, will occur at $r = 0$. This simplifies the central Bessel function term by making it a constant, Γ, that scales with the Womersley number and vial radius. Employing Euler's formula, and substituting in the expression for β, we find

$$v_{max} = v(0,t) = \frac{\Delta P_0}{i\omega\rho_f}\Gamma(\cos(\omega t) + i\sin(\omega t)) \tag{18}$$

$$= \frac{\Delta P_0}{\omega\rho_f}\Gamma(\sin(\omega t) - i\cos(\omega t)) \tag{19}$$

$$= \frac{\Delta P_0}{\omega\rho_f}\Gamma\sin(\omega t) \tag{20}$$

The pressure gradient within the fluid is assumed to be caused by the acceleration of the vial:

$$\frac{\partial P}{\partial y} = -\rho_f \alpha\omega^2 \sin(\omega t) \tag{21}$$

The amplitude of the pressure oscillation, ΔP_0, is therefore $\Delta P_0 = -\rho_f \alpha\omega^2$. Substituting into Eq. 18, we find

$$v_{max} = -\alpha\omega\Gamma\sin(\omega t). \tag{22}$$

Derivation of equation of motion

We consider the motion of the particles in the y-direction only. The force balance is given by

$$\sum F_y = ma_p = -F_g - F_d, \tag{23}$$

where F_g is the force of gravity and F_d is Stokes' drag.

Substituting into Eq. 23:

$$ma_p(t) = mv_p'(t) = my_p''(t) = -mg - 6\pi\nu r v_{rel}, \tag{24}$$

The relative velocity of the fluid, v_f, and the particle, v_{rel}, is found by:

$$v_{rel} = v_p(t) - v_f(t) = v_p(t) + \alpha\omega\Gamma\sin(\omega t), \tag{25}$$

where $v_f(t)$ is the fluid velocity, approximated as equal and opposite to the velocity of the shaking vial.

Inserting Eq. 25 into Eq. 24 and dividing by m (noting that the particle mass is given by $m = \frac{4}{3}\pi r^3 \rho_p$) produces

$$v_p'(t) = -g - kv_p(t) - k\alpha\omega\Gamma\sin(\omega t), \tag{26}$$

where k is

$$k = \frac{9}{2}\frac{\mu}{r^2\rho_p}. \tag{27}$$

Applying the Laplace transform to Eq. 26 produces

$$sV_p(s) - v_p(0) = -\frac{g}{s} - kV_p(s) - k\alpha\omega\frac{\omega}{s^2+\omega^2} \tag{28}$$

Re-arranged

$$V_p(s)(s+k) = v_p(0) - \frac{g}{s} - k\alpha\omega\frac{\omega}{s^2+\omega^2} \tag{29}$$

At $t = 0$, we assume that the velocity of the particle is equal to the peak velocity of the vial, such that

$$v_p(0) = \alpha\omega\cos(\omega\cdot 0) = \alpha\omega, \tag{30}$$

Substituting for $v_p(0)$ and isolating $V_p(s)$,

$$V_p(s) = \frac{\alpha\omega}{s+k} - \frac{g}{s(s+k)} - \frac{k\alpha\omega}{s+k}\frac{\omega}{s^2+\omega^2}. \tag{31}$$

The second and third term of the right-hand side must be reduced using the method of partial fractions. Beginning with the second term, let

$$\frac{g}{s(s+k)} = \frac{A}{s} + \frac{B}{s+k} \tag{32}$$

$$g = A(s+k) + Bs \tag{33}$$

If $s = -k$, $B = \frac{-g}{k}$; if $s = 0$, $A = \frac{g}{k}$. Therefore,

$$\frac{g}{s(s+k)} = \frac{g}{ks} - \frac{g}{k(s+k)}. \tag{34}$$

Next, we consider the third term. Let

$$\frac{k\alpha\omega^2\Gamma}{(s+k)(s^2+\omega^2)} = \frac{\eta}{s+k} + \frac{\beta s+\gamma}{s^2+\omega^2} \tag{35}$$

Re-arranging and combining yields

$$\frac{k\alpha\omega^2\Gamma}{(s+k)(s^2+\omega^2)} = \frac{\eta(s^2+\omega^2) + (\beta s+\gamma)(s+k)}{(s+k)(s^2+\omega^2)} \tag{36}$$

Expanding and grouping like terms produces

$$\frac{k\alpha\omega^2\Gamma}{(s+k)(s^2+\omega^2)} = \frac{(\eta+\beta)s^2 + (\beta k+\gamma)s + (\eta\omega^2+\gamma k)}{(s+k)(s^2+\omega^2)} \tag{37}$$

By comparison of coefficients:

$$s^2: \quad \eta+\beta = 0 \quad \Rightarrow \quad \eta = -\beta \tag{38}$$

$$s: \quad \beta k+\gamma = 0 \quad \Rightarrow \quad \beta = -\frac{\gamma}{k} \tag{39}$$

$$1: \quad \eta\omega^2 + \gamma k = k\alpha\omega^2\Gamma \tag{40}$$

Substituting in 38 and 39 into 40,

$$\frac{\gamma}{k}\omega^2 + \gamma k = k\alpha\omega^2\Gamma \tag{41}$$

$$\gamma\omega^2 + \gamma k^2 = k^s\alpha\omega^2\Gamma \tag{42}$$

$$\gamma(\omega^2+k^2) = k^2\alpha\omega^2\Gamma \tag{43}$$

$$\gamma = \frac{k^2\alpha\omega^2\Gamma}{\omega^2+k^2} \tag{44}$$

Therefore,

$$\beta = -\frac{k\alpha\omega^2\Gamma}{\omega^2+k^2} \quad \& \quad \eta = \frac{k\alpha\omega^2\Gamma}{\omega^2+k^2} \tag{45}$$

To facilitate the return to the time domain with the inverse Laplace transform, let

$$\gamma = \beta\frac{k}{\omega}. \tag{46}$$

Inserting (34) and (46) into (31), and combining like terms, yields

$$V_p(s) = \left(\alpha\omega + \frac{g}{k} - \beta\right)\frac{1}{s+k} - \frac{g}{k}\frac{1}{s} + \beta\frac{s}{s^2+\omega^2} - \beta\frac{k}{\omega}\frac{\omega}{s^2+\omega^2} \tag{47}$$

Applying the inverse Laplace transform results in

$$v_p(t) = \Phi e^{-kt} - \frac{g}{k} + \beta\cos(\omega t) - \beta\frac{k}{\omega}\sin(\omega t), \tag{48}$$

where $\Phi = \left(\alpha\omega + \frac{g}{k} - \beta\right)$.

Integrating (48) from 0 to t yields the position as a function of time:

$$y_p(t) = \int_0^t v_p(t)dt \tag{49}$$

$$
\begin{aligned}
&= \Phi \int_0^t e^{-kt} dt \\
&\quad - \frac{g}{k} \int_0^t dt \\
&\quad + \beta \int_0^t \cos(\omega t) dt \\
&\quad - \beta \frac{k}{\omega} \int_0^t \sin(\omega t) dt.
\end{aligned} \tag{50}
$$

$$
\begin{aligned}
y_p(t) = &\frac{\Phi}{k}\left(1 - e^{-kt}\right) - \frac{gt}{k} \\
&+ \frac{\beta}{\omega} \sin(\omega t) \\
&- \beta \frac{k}{\omega}(1 - \cos(\omega t)).
\end{aligned} \tag{51}
$$

Differentiating (48) results in the acceleration:

$$
a_p(t) = v_p'(t) = -k\Phi e^{-kt} - \beta\omega \sin(\omega t) - \beta k \cos(\omega t). \tag{52}
$$

Acknowledgements The authors would like to acknowledge F. McDonald and B. Lomax for hosting V. Schein in their labs at ESTEC, and for allowing us to include this study as an addendum to their work with lunar regolith sample 15601.

Author contributions J.N.R contributed toward conceptualisation, lab supervision, numerical modelling, data analysis, writing—original draft, and writing—review and editing. L.E.S-F. contributed toward X-Ray CT methodology, investigation, data analysis, writing—original draft, and writing—review and editing. S.O.S contributed toward conceptualisation, numerical modelling, data analysis, and writing—review and editing. V.S contributed toward conceptualisation, experimental methodology, investigation, and data analysis. B.L. contributed toward conceptualisation, experimental methodology, and investigation. F.M. contributed toward conceptualisation, experimental methodology, and investigation. J.J.C. contributed toward supervision and writing—review and editing. K.H. contributed toward supervision and writing—review and editing.

Funding The authors acknowledge that they received no external funding in support for this research.

Data availability The processed data from the micro-CT analysis used in the quantification of the particle size distributions (Figs. 3–6) are publicly available in the Zenodo repository at 10.5281/zenodo.15697405. Due to size limitations, micro-CT reconstructions are stored offline and may be made available upon request.

Declarations

Conflict of interest The authors declare no Conflict of interest.

Open Access This article is licensed under a Creative Commons Attribution 4.0 International License, which permits use, sharing, adaptation, distribution and reproduction in any medium or format, as long as you give appropriate credit to the original author(s) and the source, provide a link to the Creative Commons licence, and indicate if changes were made. The images or other third party material in this article are included in the article's Creative Commons licence, unless indicated otherwise in a credit line to the material. If material is not included in the article's Creative Commons licence and your intended use is not permitted by statutory regulation or exceeds the permitted use, you will need to obtain permission directly from the copyright holder. To view a copy of this licence, visit http://creativecommons.org/licenses/by/4.0/.

References

Arens, E., Starr, S.: Mechanical measurements on powdered cryogenic insulations; perlite and 3m glass bubbles, Unpublished Internal Memo. Kennedy Space Center Applied Physics Lab (2012)

Asmar, B., Langston, P., Matchett, A.: A generalised mixing index in distinct element method simulation of vibrated particulate beds. Granular Matter **4**, 129–138 (2002). https://doi.org/10.1007/s10035-002-0112-8

Basu, A., McKay, D. S., Nace, G., Griffiths, S. A.: Petrography of lunar soil 15601. In: Proc. 11th Lunar Planet. Sci. Conf. , pp. 1727–1741 (1980).

Balista, J.A.F., Juanico, D.E.O., Saloma, C.A.: The Brazilian nut effect by void filling: an analytic model. Complexity **16**, 9–16 (2011). https://doi.org/10.1002/cplx.20345

Brown, D., Hanson, R., Christian, W.: Tracker video analysis and modeling tool, 2024. Version 6.2.0

Calle, C.I.: Electrostatic Phenomena on Planetary Surfaces. Morgan & Claypool Publishers, San Rafael (2017)

Captain, J., Trigwell, S., Arens, E., Biris, A., Captain, J., Quinn, J., Calle, C.: Tribocharging lunar simulant in vacuum for electrostatic beneficiation. In: AIP Conference Proceedings, volume 880, AIP, pp. 951–956 (2007)

Carrier III, W.D.: The four things you need to know about the geotechnical properties of lunar soil (2005)

Carrier III, W. D., Mitchell, J. K., Mahmood, A.: The relative density of lunar soil. In: Lunar and Planetary Science Conference Proceedings, volume 4, p. 2403 (1973)

Chujo, T., Mori, O., Kawaguchi, J., Yano, H.: Categorization of brazil nut effect and its reverse under less-convective conditions for microgravity geology. Mon. Not. R. Astron. Soc. **474**, 4447–4459 (2017). https://doi.org/10.1093/mnras/stx3092

Ciamarra, M.P., Domenica De Vizia, M., Fierro, A., Tarzia, M., Coniglio, A., Nicodemi, M.: Granular species segregation under vertical tapping: effects of size, density, friction, and shaking amplitude. Phys. Rev. Lett. **96**, 058001 (2006). https://doi.org/10.1103/PhysRevLett.96.058001

Cilliers, J., Hadler, K., Rasera, J.: Toward the utilisation of resources in space: knowledge gaps, open questions, and priorities. npj Microgravity **9**, 22 (2023)

Cilliers, J.J., Rasera, J.N., Hadler, K.: Estimating the scale of space resource utilisation (SRU) operations to satisfy lunar oxygen demand. Planet. Space Sci. **180**, 104749 (2020)

Cover, T.M.: Elements of Information Theory. Wiley, Hoboken (1999)

Dippel, S., Luding, S.: Simulation on size segregation: geometrical effects in the absence of convection. J. Phys. I **5**, 1527–1537 (1995). https://doi.org/10.1051/jp1:1995215

Dotson, B., Valencia, D.S., Millwater, C., Easter, P., Long-Fox, J., Britt, D., Metzger, P.: Cohesion and shear strength of compacted lunar and martian regolith simulants. Icarus **411**, 115943 (2024)

Duran, J., Mazozi, T., Clément, E., Rajchenbach, J.: Size segregation in a two-dimensional sandpile: convection and arching effects. Phys. Rev. E **50**, 5138–5141 (1994). https://doi.org/10.1103/PhysRevE.50.5138

Duran, J., Rajchenbach, J., Clément, E.: Arching effect model for particle size segregation. Phys. Rev. Lett. **70**, 2431–2434 (1993). https://doi.org/10.1103/PhysRevLett.70.2431
Duran, J.: Sands, Powders, and Grains: An Introduction to the Physics of Granular Materials. Springer, Berlin (2012)
Gajjar, P., Johnson, C.G., Carr, J., Chrispeels, K., Gray, J.M.N.T., Withers, P.J.: Size segregation of irregular granular materials captured by time-resolved 3D imaging. Sci. Rep. **11**, 8352 (2021). https://doi.org/10.1038/s41598-021-87280-1
Graf J.C.: Lunar soils grain size catalog. NASA Pub, Washington, 1265 (1993)
Godoy, S., Risso, D., Soto, R., Cordero, P.: Rise of a brazil nut: a transition line. Phys. Rev. E **78**, 031301 (2008). https://doi.org/10.1103/PhysRevE.78.031301
Good, P.: Permutation Tests: A Practical Guide to Resampling Methods for Testing Hypotheses. Springer, Berlin (2013)
Hsiau, S., Yu, H.: Segregation phenomena in a shaker. Powder Technol **93**, 83–88 (1997). https://doi.org/10.1016/S0032-5910(97)03263-4
Hu, J., Pei, C., Zhang, L., Liang, C., Wu, C.Y.: Numerical analysis of frictional charging and electrostatic interaction of particles. AIChE J (2021). https://doi.org/10.1002/aic.17444
Huerta, D.A., Ruiz-Suárez, J.C.: Vibration-induced granular segregation: a phenomenon driven by three mechanisms. Phys. Rev. Lett. **92**, 114301 (2004). https://doi.org/10.1103/PhysRevLett.92.114301
John, K.K., Rogers, C.E.: Classifications and Requirements for Testing Systems and Hardware to be Exposed to Dust in Planetary Environments. Technical Report, NASA (2021)
Jullien, R., Meakin, P., Pavlovitch, A.: Three-dimensional model for particle-size segregation by shaking. Phys. Rev. Lett. **69**, 640–643 (1992). https://doi.org/10.1103/PhysRevLett.69.640
Kawamoto, H., Chin, K.: Particle-size classification of lunar regolith through inclined vibrating tube. J. Aerosp. Eng. **34**, 06021003 (2021)
Knight, J.B., Jaeger, H.M., Nagel, S.R.: Vibration-induced size separation in granular media: the convection connection. Phys. Rev. Lett. **70**, 3728–3731 (1993). https://doi.org/10.1103/PhysRevLett.70.3728
Kobaka, J., Katzer, J., Seweryn, K., Srokosz, P., Bujko, M., Konečnỳ, P.: A study of lunar soil simulants from construction and building materials perspective. Case Stud. Construct. Mater. **18**, e02082 (2023)
Kornuta, D., Abbud-Madrid, A., Atkinson, J., Barr, J., Barnhard, G., Bienhoff, D., Blair, B., Clark, V., Cyrus, J., DeWitt, B., Dreyer, C., Finger, B., Goff, J., Ho, K., Kelsey, L., Keravala, J., Kutter, B., Metzger, P., Montgomery, L., Morrison, P., Neal, C., Otto, E., Roesler, G., Schierr, J., Seifert, B., Sowers, G., Spudis, P., Sundahl, M., Zacny, K., Zhu, G.: Commercial lunar propellant architecture: a collaborative study of lunar propellant production. Reach **13**, 100026 (2019)
Lab, E.: 2023. https://cdn.shopify.com/s/files/1/0398/9268/0862/files/lms-1-spec-sheet-June2023.pptx.pdf?v=1688054883
Li, T., Ban, H., Hower, J., Stencel, J., Saito, K.: Dry triboelectrostatic separation of mineral particles: a potential application in space exploration. J. Electrost. **47**, 133–142 (1999)
Liao, C.C.: Multisized immersed granular materials and bumpy base on the brazil nut effect in a three-dimensional vertically vibrating granular bed. Powder Technol **288**, 151–156 (2016). https://doi.org/10.1016/j.powtec.2015.10.054
Linke, S., Windisch, L., Kueter, N., Wanvik, J.E., Voss, A., Stoll, E., Schilde, C., Kwade, A.: Tubs-m and tubs-t based modular regolith simulant system for the support of lunar isru activities. Planet. Space Sci. **180**, 104747 (2020)
Long-Fox, J.M., Landsman, Z.A., Easter, P.B., Millwater, C.A., Britt, D.T.: Geomechanical properties of lunar regolith simulants LHS-1 and LMS-1. Advances in Space Research **71**, 5400–5412 (2023)
Long-Fox, J.M., Britt, D.T.: Characterization of planetary regolith simulants for the research and development of space resource technologies. Frontiers in Space Technologies **4**, 1255535 (2023)
Maurel, C., Ballouz, R.L., Richardson, D.C., Michel, P., Schwartz, S.R.: Numerical simulations of oscillation-driven regolith motion: Brazil-nut effect. Mon. Not. R. Astron. Soc. **464**, 2866–2881 (2016). https://doi.org/10.1093/mnras/stw2641
McKay, D.S., Heiken, G., Basu, A., Blanford, G., Simon, S., Reedy, R., French, B.M., Papike, J.: The Lunar Regolith. In: Lunar Sourcebook. Cambridge University Press, New York (1991)
McKay, D.S., Carter, J.L., Boles, W.W., Allen, C.C., Allton, J.H.: Jsc-1: a new lunar soil simulant. Engineering, construction, and operations in space IV **2**, 857–866 (1994)
Meyer, C.: Soil sample 15601, The Lunar Sample Compendium (2011). https://curator.jsc.nasa.gov/lunar/lsc/15601.pdf
Metzger, M.J., Remy, B., Glasser, B.J.: All the brazil nuts are not on top: vibration induced granular size segregation of binary, ternary and multi-sized mixtures. Powder Technol **205**, 42–51 (2011). https://doi.org/10.1016/j.powtec.2010.08.062
Möbius, M.E., Lauderdale, B.E., Nagel, S.R., Jaeger, H.M.: Size separation of granular particles. Nature (2001). https://doi.org/10.1038/35104697
Morris, R.: The surface exposure/maturity/of lunar soils-some concepts and is/FeO compilation. In: Lunar and Planetary Science Conference, 9th, Houston, Tex., March 13–17, 1978, Proceedings. Volume 2 (A79-39176 16-91), pp. 2287-2297., volume. 9 Pergamon Press, Inc., New York (1978).
Morris, R.V.: Handbook of lunar soils. Lyndon B, Johnson Space Center (1983)
Moore, C., Lewis, C. Gibson Jr, E.: Total carbon contents of apollo 15 and 16 lunar samples. In: Proceedings of the Lunar Science Conference, vol. 4, p. 1613, volume 4, p. 1613 (1973)
Nielsen, F.: On a generalization of the Jensen-Shannon divergence and the Jensen-Shannon centroid. Entropy **22**, 221 (2020)
Nielsen, J.: Pressures from flowing granular solids in silos, philosophical transactions of the royal society of london. Ser. A Math., Phys. Eng. Sci. **356**, 2667–2684 (1998)
Otsu, N.: A threshold selection method from gray-level histograms. IEEE Trans. Syst. Man Cybern. **9**, 62–66 (1979)
Plitt, L., Kawatra, S.: Estimating the cut (d50) size of classifiers without product particle-size measurement. Int. J. Miner. Process **5**(5), 369–378 (1979)
Poeschel, T., Herrmann, H.: Size segregation and convection. Europhys. Lett. **29**, 123 (1995). https://doi.org/10.1209/0295-5075/29/2/003
Pukkella, A.K., Cilliers, J.J., Hadler, K.: A comprehensive review and recent advances in dry mineral classification. Miner. Eng. **201**, 108208 (2023)
Quinn, J.W., Captain, J.G., Weis, K., Santiago-Maldonado, E., Trigwell, S.: Evaluation of tribocharged electrostatic beneficiation of lunar simulant in lunar gravity. J. Aerosp. Eng. **26**, 37–42 (2012)
Rasera, J., Cilliers, J.J., Lamamy, J.-A., Hadler, K.: The beneficiation of lunar regolith for space resource utilisation: a review. Planet. Space Sci. **186**, 104879 (2020)
Rasera, J., Cruise, R., Cilliers, J., Lamamy, J.-A., Hadler, K.: Modelling the tribocharging process in 2D and 3D. Powder Technol **407**, 117607 (2022)
Rasera, J., Cilliers, J., Lamamy, J.-A., Hadler, K.: A methodology for tribocharger design optimisation using the discrete element method (DEM). Powder Technol. **413**, 118035 (2023)
Rasera, J., Cilliers, J., Lamamy, J.-A., Hadler, K.: Experimental investigation of an optimised tribocharger design for space resource utilisation. Planet. Space Sci. **228**, 105651 (2023)

Rosato, A.D., Blackmore, D.L., Zhang, N., Lan, Y.: A perspective on vibration-induced size segregation of granular materials. Chem. Eng. Sci. **57**, 265–275 (2002). https://doi.org/10.1016/S0009-2509(01)00380-3

Rosato, A., Strandburg, K.J., Prinz, F., Swendsen, R.H.: Why the brazil nuts are on top: size segregation of particulate matter by shaking. Phys. Rev. Lett. **58**, 1038–1040 (1987). https://doi.org/10.1103/PhysRevLett.58.1038

Saez, A., Vivanco, F., Melo, F.: Size segregation, convection, and arching effect. Phys. Rev. E **72**, 021307 (2005). https://doi.org/10.1103/PhysRevE.72.021307

Sanders, D.A., Swift, M.R., Bowley, R.M., King, P.J.: Are brazil nuts attractive? Phys. Rev. Lett. **93**, 208002 (2004). https://doi.org/10.1103/PhysRevLett.93.208002

Shaw, M., Humbert, M., Brooks, G., Rhamdhani, A., Duffy, A., Pownceby, M.: Mineral processing and metal extraction on the lunar surface-challenges and opportunities. Miner. Process. Extr. Metall. Rev. **43**, 865–891 (2022)

Shinbrot, T.: The brazil nut effect—in reverse. Nature **429**, 352–353 (2004). https://doi.org/10.1038/429352b

Shinbrot, T., Muzzio, F.J.: Reverse buoyancy in shaken granular beds. Phys. Rev. Lett. **81**, 4365–4368 (1998). https://doi.org/10.1103/PhysRevLett.81.4365

Skilling, J., Bryan, R.: Maximum entropy image reconstruction-general algorithm. Monthly Not. R. Astron. Soc. **211**(1), 111 (1984) 111

Trigwell, S., Captain, J.G., Arens, E.E., Quinn, J.W., Calle, C.I.: The use of tribocharging in the electrostatic beneficiation of lunar simulant. IEEE Trans. Ind. Appl. **45**, 1060–1067 (2009)

Taylor, L.A., Carrier III, W.D.: Oxygen production on the moon: an overview and evaluation. Resources of Near-Earth Space **69** (1993)

Trigwell, S., Captain, J., Arens, E., Captain, J., Quinn, J., Calle, C.: The use of tribocharging in the electrostatic beneficiation of lunar simulant. In: Physics Electrostatics 2007 Conference, KSC-2007-013 (2007)

Trigwell, S., Captain, J., Captain, J., Arens, E., Quinn, J., Calle, C.: Electrostatic Beneficiation of Lunar Simulant. Report, NASA (2006)

Trigwell, S., Captain, J., Weis, K., Quinn, J.: Electrostatic beneficiation of lunar regolith: applications in in situ resource utilization. J. Aerosp. Eng. **26**, 30–36 (2012)

Vanel, L., Rosato, A.D., Dave, R.N.: Rise-time regimes of a large sphere in vibrated bulk solids. Phys. Rev. Lett. **78**, 1255–1258 (1997). https://doi.org/10.1103/PhysRevLett.78.1255

Williams, J.C.: The segregation of powders and granular materials. Fuel Soc. J. **14**, 29–34 (1963)

Willman, B.M., Boles, W.W., McKay, D.S., Allen, C.C.: Properties of lunar soil simulant jsc-1. J. Aerosp. Eng. **8**, 77–87 (1995)

Williams, R.J., McKay, D.S., Giles, D., Bunch, T.E.: Mining and beneficiation of lunar ores. Space Resources and Space Settlements 275–288 (1979)